




# Imaging multilevel exciton transport enabled by correlated electronic states

Received: 5 July 2025

Accepted: 14 January 2026

Published online: 29 January 2026

 Check for updates

Huan Liu  , Shihong Chen, Haowen Xu, Rui Han, Zejun Sun, Shuchun Huang, Xiushuo Zhang, Li Huang, Jianbin Luo  & Dameng Liu  

Exciton transport is a fundamental energy transfer process essential to semiconductor optoelectronic devices, whose full application potential relies critically on achieving precise multilevel control. While correlated electronic states in transition metal dichalcogenides (TMDCs) offer unprecedented tunability, probing exciton dynamics within these states has been challenging due to limitations in the spatial and temporal resolution of conventional techniques. Here, we introduce an ultrafast optical imaging approach, integrating femtosecond transient absorption microscopy with a WSe<sub>2</sub> exciton sensor near twisted WS<sub>2</sub> moiré superlattices, achieving 200 fs temporal and 50 nm spatial resolution. Within these moiré systems, the formation of generalized Wigner crystals induces multilevel exciton transport by substantially altering the local dielectric environment, which in turn significantly reduces exciton lifetime and diffusion. Our findings reveal how correlated electronic states regulate exciton dynamics and establish a dynamic control framework with profound implications for next-generation logic computing, photonic interconnects, and optical modulation technologies.

Exciton transport in two-dimensional transition metal dichalcogenides (TMDCs) plays a critical role as the core process for optical and electrical signal interconversion<sup>1–8</sup>. Featuring ultrafast switching operation and minimal static power consumption, it holds great promise for enabling complex logic processing, neuromorphic computing, and integrated excitonic circuits in future technologies<sup>9–19</sup>. To realize these applications, devices go beyond a binary on/off response: they require stable, addressable multilevel states—discrete transport levels between the fully suppressed and fully diffusive limits—while remaining compatible with on-chip optoelectronic interconnects. The key to realizing these excitonic applications lies in the precise and dynamic control of exciton transport<sup>20–28</sup>. Current control methods—including electric fields, strain, dielectric environment, and twist angles—typically rely on fixed parameters and lack the flexibility for dynamic tuning. Fortunately, in recent years, the discovery of rich correlated electronic states in two-dimensional materials has opened new possibilities<sup>29–39</sup>. By doping different fractional carrier densities, materials can switch between correlated insulating and metallic states. If these rich correlated electronic

states could be harnessed as a control mechanism for exciton transport, it would enable multi-level exciton transport modulation—an area that remains largely unexplored.

A key obstacle in studying exciton transport in these correlated electronic states is the lack of probes that combine both high spatial resolution and temporal resolution while preserving fragile correlated states. Conventional electrical transport measurements suffer from high contact resistance and signal averaging across an entire sample, which can obscure local and ultrafast dynamics. Some noninvasive techniques, such as exciton sensors and scanning tunneling microscopy, have provided important insights into fragile correlated states<sup>29,31,32,35,38–46</sup>, but still lack the temporal resolution to capture real-time exciton transport. Overcoming this limitation requires a method that can simultaneously resolve spatial and temporal features, which is essential for revealing the underlying exciton transport dynamics in correlated electronic states.

In this study, we develop an optical imaging technique that integrates femtosecond transient absorption microscopy with an exciton

State Key Laboratory of Tribology in Advanced Equipment, Department of Mechanical Engineering, Tsinghua University, Beijing, China.

 e-mail: [liuhuan122@mail.tsinghua.edu.cn](mailto:liuhuan122@mail.tsinghua.edu.cn); [luojb@mail.tsinghua.edu.cn](mailto:luojb@mail.tsinghua.edu.cn); [ldm@tsinghua.edu.cn](mailto:ldm@tsinghua.edu.cn)

sensor, enabling exciton transport measurements with 200 femtosecond time resolution and 50 nanometers spatial resolution (Fig. 1a). In our design, the electric field line from electron-hole pairs in the  $\text{WSe}_2$  sensor extends through a thin spacer, partially reaching the adjacent twisted  $\text{WS}_2$  moiré superlattice. As a result, the exciton transport in the  $\text{WSe}_2$  is strongly influenced by the generalized Wigner crystals in the  $\text{WS}_2$  bilayer. When the moiré system is in a metallic state, the surrounding hexagonal boron nitride (hBN) effectively screens dielectric disorders, smoothing local potential fluctuations and enhancing exciton transport in  $\text{WSe}_2$ . In contrast, when the moiré system enters a Wigner insulating state, its dielectric constant drops sharply, leading to increased dielectric disorder that suppresses exciton transport. These

results establish an ultrafast optical method for probing exciton dynamics in quantum materials and offer a versatile platform for studying light-matter interactions in Bose-Fermi mixture systems.

## Results

### Device design

The device consists of a monolayer  $\text{WSe}_2$  sensor placed below twisted  $\text{WS}_2$  bilayers, separated by a thin ( $\sim 1$  nm) hBN spacer. This spacer preserves proximity while minimizing electronic coupling, allowing effective optical detection of nearby correlated electronic states. In this configuration, the generalized Wigner crystals in  $\text{WS}_2$  bilayers can effectively interact with the exciton transport in  $\text{WSe}_2$ . An optical

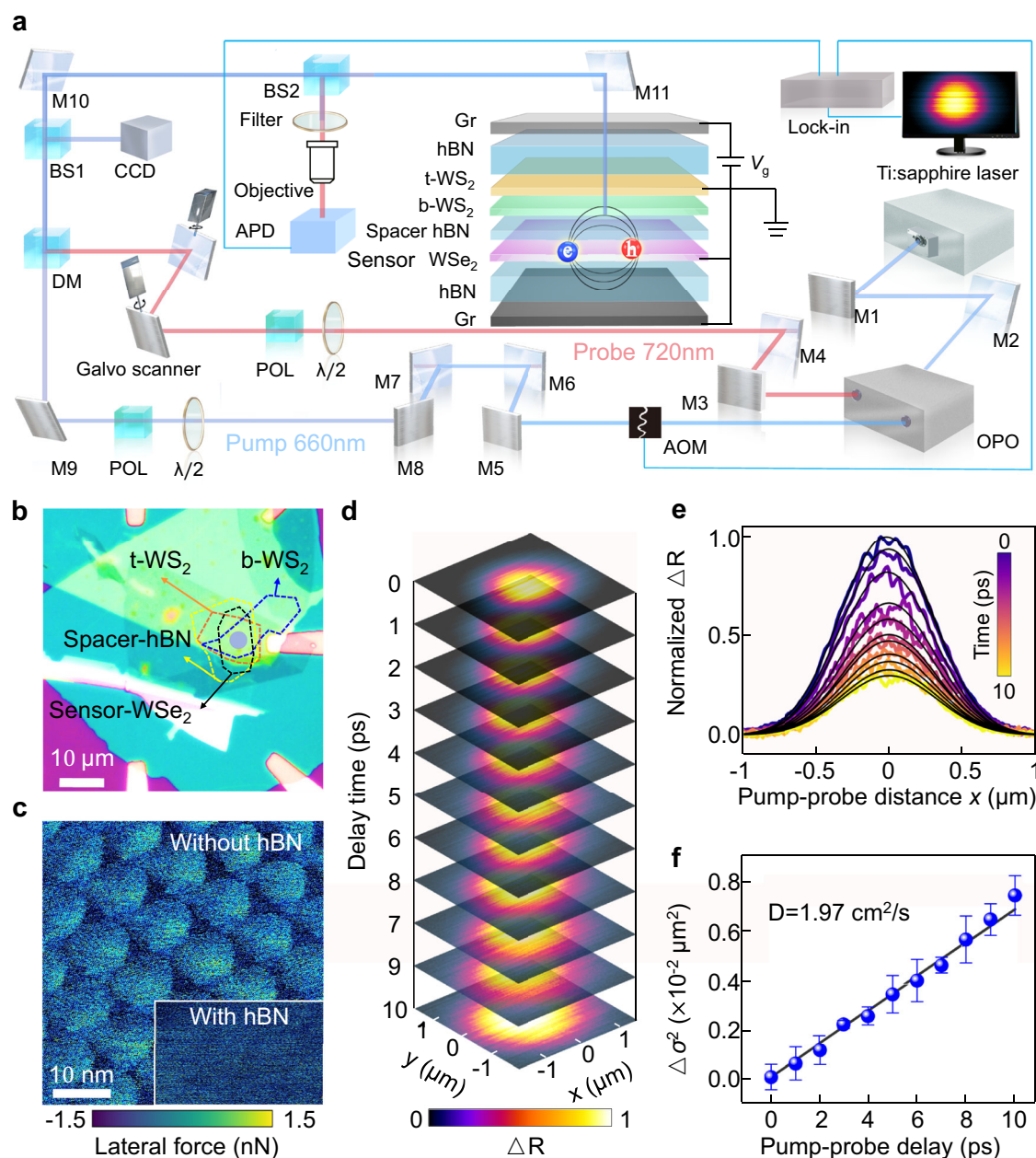


**Fig. 1 | Device structure and measurement scheme.** **a** Schematic of an optical imaging technique integrating femtosecond transient absorption microscopy with an exciton sensor for ultrafast exciton dynamics (Methods). **b** Optical image of the fabricated device. The dot indicates the position of the pump-probe measurement spot. **c** Lateral friction force map of twisted  $\text{WS}_2$  bilayers with an interlayer twist angle of  $58^\circ$ , resulting in a 9.2 nm moiré pattern. The moiré pattern becomes

negligible when isolated by an hBN spacer (inset). **d** Two-dimensional exciton transport images at a gate voltage  $V_g = 0$ . **e** Exciton population profiles as a function of pump-probe distance  $x$ , fitted via a Gaussian function. **f** Relationship between the mean squared displacement  $\Delta\sigma^2(t)$  and time, allowing the extraction of  $D$  through the relation  $\Delta\sigma^2(t) = 4Dt$ . The error bar denotes the standard deviation across the three Gaussian-fit results.

image of the device is shown in Fig. 1b, with further characterization in Supplementary Fig. 1. The WS<sub>2</sub> bilayers, twisted at an interlayer angle of 58°, form a moiré pattern with a periodicity of approximately 9.2 nm (Fig. 1c), whereas the spacer largely suppresses moiré effects in WSe<sub>2</sub> (inset, Fig. 1c). The full heterostructure is encapsulated in ~48 nm thick hBN layers, with few-layer graphite electrodes on both sides. Both the WSe<sub>2</sub> and WS<sub>2</sub> bilayers are electrically grounded to ensure charge neutrality of WSe<sub>2</sub> (Supplementary Fig. 2). By tuning the carrier doping in the WS<sub>2</sub> moiré superlattice, the system can be driven from a metallic state to a generalized Wigner insulating state, thereby modifying the local dielectric environment<sup>29</sup> and influencing exciton transport in the WSe<sub>2</sub> layer<sup>25</sup>.

We visualize exciton transport in Wigner crystals using ultrafast pump-probe microscopy<sup>47,48</sup>. A pump pulse at 660 nm selectively excites the WSe<sub>2</sub> layer without affecting the WS<sub>2</sub> bilayers, as this wavelength lies below the WS<sub>2</sub> bandgap (Supplementary Fig. 3). This selective excitation minimizes disturbance to the correlated electronic states in the twisted WS<sub>2</sub> moiré superlattices. A probe pulse at 720 nm then monitors intralayer exciton transport in the WSe<sub>2</sub> layer by measuring the pump-induced reflection change,  $\Delta R(x, y, t)$ , which is proportional to the exciton density,  $n(x, y, t)$ . Because the electric field from the photoexcited electron-hole pairs in WSe<sub>2</sub> extends into the adjacent moiré layers, exciton transport is highly responsive to the surrounding dielectric environment. Typically, in regions with higher state dielectric constants, Coulomb scattering is suppressed and dielectric disorder is reduced<sup>25,49</sup>, leading to enhanced exciton transport. Consequently, exciton transport in WSe<sub>2</sub> serves as a powerful optical probe for the dielectric properties of the neighboring twisted WS<sub>2</sub> moiré superlattice.

### Imaging exciton transport

To track the spatial and temporal evolution of exciton transport, we keep the pump beam fixed while scanning the probe beam across it at varying delay times. Fig. 1d presents two-dimensional images of exciton transport at a gate voltage  $V_g = 0$ , revealing the expansion of the exciton population over time. For quantitative analysis, we assume a radially symmetric exciton distribution following a Gaussian profile. At time zero, the excitons are generated by the pump beam with an initial spot size of approximate 1  $\mu\text{m}$ , described by  $n(x, 0) = n_0 \exp(-x^2/\sigma_0^2)$ . At later times, the exciton population profiles are fitted by the Gaussian function  $n(x, t) = n_t \exp(-x^2/\sigma_t^2)$ , as shown by the solid lines in Fig. 1e. Exciton transport is characterized by the mean squared displacement, calculated as  $\Delta\sigma^2(t) = \sigma^2(t) - \sigma^2(0)$ . The spatial resolution is defined by the exciton transport's resolvable cutoff, achieving 50 nm. Unless otherwise specified, all measurements are performed at a temperature of 10 K.

We extract the exciton diffusion coefficient ( $D$ ) in the WSe<sub>2</sub> using a standard diffusion model described by  $\partial n(x, t)/\partial t = D\nabla^2 n(x, t) - n(x, t)/\tau$ , where  $n$  is the exciton density and  $\tau$  is the exciton lifetime. As shown in Fig. 1f, the mean squared displacement  $\Delta\sigma^2(t)$  increases linearly with time, allowing to extract  $D$  using the relation  $\Delta\sigma^2(t) = 4Dt$ . The linear time dependence of WSe<sub>2</sub> exciton diffusion reflects the action of the thin hBN spacer, which screens the WS<sub>2</sub> moiré potential so that WSe<sub>2</sub> excitons do not experience periodic trapping. The hBN spacer is thinner than the Bohr radius of a 1s exciton (~1.7 nm)<sup>39,50</sup>, ensuring that the Wigner insulating states in WS<sub>2</sub> bilayers effectively regulate exciton transport in WSe<sub>2</sub>. This structural design allows us to focus purely on the influence of electronic correlated states on exciton dynamics. Notably, the initial photoinjected exciton density is maintained at  $\sim 1 \times 10^{11} \text{ cm}^{-2}$ , which is sufficiently low to avoid exciton-exciton annihilation and electron-hole plasma effects (Supplementary Fig. 4). All measurements reported in this work are therefore performed in the low-exciton-density regime, which provides the baseline for discussing the influence of dielectric disorder on exciton transport<sup>49,51</sup>.

### Exciton transport sensing of Wigner crystals

We next investigate how the exciton transport in the WSe<sub>2</sub> sensor responds to gate-tuned changes in the dielectric environment of the adjacent WS<sub>2</sub> moiré bilayer, measured at a fixed delay time of 5 ps (Fig. 2a and Supplementary Fig. 5). By tuning the gate voltage  $V_g$ , the WS<sub>2</sub> moiré system transitions can be switched between metallic and Wigner insulating states, which modifies its electronic density of states and, in turn, its dielectric constant<sup>35,40,41</sup>. These changes directly affect the exciton transport behavior in the adjacent WSe<sub>2</sub> layer (Fig. 2b). Specifically, excitons in monolayer transition metal dichalcogenides experience strong Coulomb interactions and reduced dielectric screening, leading to their binding electrostatic field lines extending largely outside the monolayer. This makes excitons strongly influenced by changes in the surrounding dielectric environment<sup>25</sup>. An external environment with a high dielectric constant can enhance exciton transport by suppressing the Coulomb scattering effect from dielectric disorders<sup>52</sup>. To verify this conclusion, we fabricated a large-angle and a monolayer control device, in which no suppression of exciton transport is observed at fractional filling factors (Supplementary Figs. 6 and 7).

Furthermore, in the moiré superlattice, the dielectric response is approximately proportional to its electronic density of states<sup>29</sup>, which reflects the compressibility of the twisted WS<sub>2</sub>. This configuration allows the WSe<sub>2</sub> monolayer to serve as an optical probe for detecting correlated electronic states in twisted WS<sub>2</sub> moiré superlattices. When the moiré superlattice is metallic and compressible, it exhibits a large dielectric constant that suppresses Coulomb scattering with dielectric disorder, leading to significant exciton transport. In contrast, when the system enters a correlated insulating (incompressible) state, the dielectric constant decreases, weakening this suppression and causing a sharp reduction in exciton transport.

We then examine the temporal dynamics of exciton transport at different filling factors. Fig. 2c shows how the exciton population evolves in space over time for the filling factors  $\nu = 0, 1/2$ , and  $2/3$  (three-dimensional rotation results shown in Supplementary Movie 1). Compared with the undoped case ( $\nu = 0$ ), exciton transport is notably reduced at fractional fillings due to the formation of Wigner crystals. At these fractional fillings, strong inter-site Coulomb interactions drive electrons to arrange in ordered patterns that minimize the total potential energy, resulting in wavefunction localization and a breakdown of translational symmetry in the moiré superlattice. Specifically, the filling factors  $\nu = 1/3$  or  $2/3$  give rise to triangular lattice arrangements, whereas  $\nu = 1/2$  forms a stripe-like lattice phase<sup>34</sup>. This electron localization significantly decreases the dielectric constant of the WS<sub>2</sub> moiré superlattice, reducing its ability to screen dielectric disorder in the adjacent WSe<sub>2</sub> layer and consequently suppress exciton transport.

Figure 2d displays the exciton diffusion coefficients across various filling factors, revealing stepwise transport behavior (with detailed analysis provided in Supplementary Figs. 8–12). In the metallic state, the exciton diffusion coefficient remains nearly constant, indicating that increased carrier doping within WS<sub>2</sub> moiré superlattices has little effect on exciton transport. This stability suggests that exciton transport in WSe<sub>2</sub> is governed mainly by the dielectric properties of the adjacent WS<sub>2</sub> bilayers, which remain relatively constant at low doping levels (Methods). In contrast, at fractional fillings, the diffusion coefficient sharply decreases due to the presence of Wigner insulating states. Notably, the diffusion coefficients at  $\nu = 1/3$  and  $2/3$  are comparable and smaller than those at  $\nu = 1/2$ . This difference arises from the weaker interactions at  $\nu = 1/2$ , where reduced Coulomb interactions and longer exciton lifetimes enhance dielectric screening and partially preserve exciton transport. Exciton transport on the hole-doped side shows behavior similar to that on the electron-doped side. For both cases, the diffusion coefficients at the fractional filling factor  $\nu$  closely match those at the complementary values ( $\nu - 1/2$ ), indicating a symmetric response around half-filling. These distinct changes in

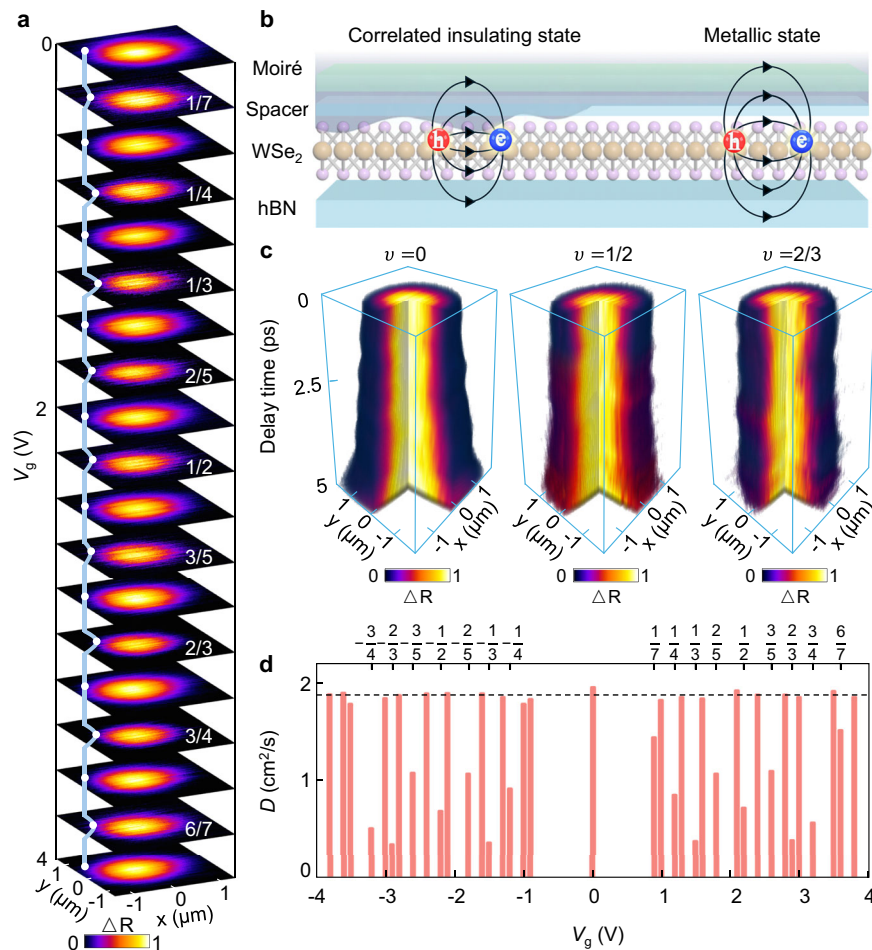


**Fig. 2 | Imaging exciton transport sensing of Wigner crystals.** **a** Exciton transport under varying doping in the WS<sub>2</sub> bilayer, measured at a fixed delay time of 5 ps. At fractional filling factors, exciton transport is suppressed. **b** Schematic illustrating the mechanism of Wigner crystal-mediated exciton transport. In the metallic state, the WS<sub>2</sub> bilayer exhibits low dielectric disorder, enhancing transport; in the

correlated state, increased dielectric suppresses transport. **c** Time-dependent exciton transport for filling factors of  $\nu = 0, 1/2$ , and  $2/3$ . Compared with the zero-filling case, exciton transport is significantly suppressed due to the formation of Wigner crystals. **d** Exciton diffusion coefficients as a function of different filling factors, exhibiting stepwise transport behavior.

exciton transport highlight the sensitivity of our optical method to the formation of generalized Wigner crystals. This exciton-transport sensing method provides a time-resolved probe of correlated electronic states. Consistently, we observe the same conclusion in another independent device (Supplementary Figs. 13–18). In addition to the fractional fillings discussed in the manuscript, we also observe a pronounced suppression of exciton diffusion at the integer fillings  $\nu = \pm 1$  (Supplementary Fig. 19). These insulating states are consistent with well-established Mott insulators<sup>29,53</sup>.

### Exciton lifetime and diffusion length

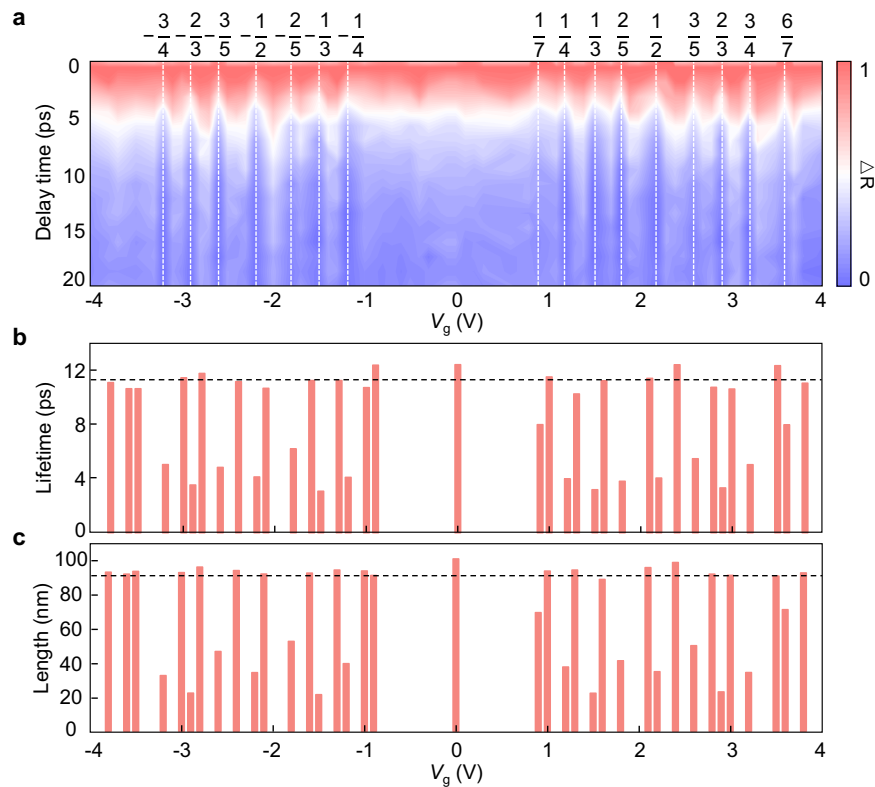
Wigner insulating states also influence exciton lifetimes. As shown in Fig. 3a, exciton decay remains nearly unchanged in the metallic state. However, at fractional fillings corresponding to generalized Wigner insulating states, the exciton lifetime decreases sharply (Methods). This reduction arises because the insulating states reduce the dielectric constant of the WS<sub>2</sub> bilayers, thereby reducing the dielectric screening of excitons in WSe<sub>2</sub>. Consequently, the exciton binding energy increases, leading to greater electron-hole wavefunction overlap and a shorter exciton lifetime.

Figure 3b further illustrates how the exciton lifetime varies with the filling factor, closely following the trend observed in the exciton diffusion coefficients. Representative exciton lifetime decay curves are presented in Supplementary Fig. 20. The exciton diffusion length,

defined as  $L = 2\sqrt{D\tau}$  depends on both the exciton lifetime and the diffusion coefficient. Fig. 3c illustrates the dependence of the exciton diffusion length on doping, revealing a significant reduction at the fractional filling factor. This reduction contrasts with the observation of interlayer exciton transport in moiré lattices, where the reduced diffusion length at fractional fillings is often compensated by increased lifetimes<sup>54</sup>. In our case, both the diffusion coefficient and the lifetime decrease simultaneously, resulting in more pronounced suppression of transport and providing a clear optical signature of correlated electronic states.

### Temperature dependence

Finally, we investigate the temperature dependence of exciton transport in Wigner crystals in Fig. 4a (with detailed analysis provided in Supplementary Figs. 21–25). At low temperatures (10–25 K), exciton transport is notably suppressed at fractional fillings (Supplementary Movie 2). As the temperature rises to the range of 30–45 K, this suppression gradually weakens and eventually disappears, indicating that the generalized Wigner crystals no longer regulate exciton transport. For each correlated electronic state, we identify a critical temperature ( $T_c$ ) at which this suppression is lifted (Fig. 4b). At a fixed filling factor  $\nu$ , we evaluate the strength of the insulating state by measuring the suppression of exciton transport relative to a nearby compressible background. We define the critical temperature  $T_c$  as the temperature



**Fig. 3 | Doping-dependent exciton lifetime and diffusion length.** **a** Transient reflectance map  $\Delta R(t, V_g)$  versus pump-probe delay  $t$  and gate voltage  $V_g$ . The vertical dashed lines (labels on top) mark the fractional fillings  $\nu$  determined from the calibration described in the Methods section. At these fillings, the signal decays faster, indicating a shortened exciton lifetime, whereas away from them (metallic regime), the decay is slower and nearly uniform. Each trace is normalized to its own maximum absolute value within the analysis window. **b** Exciton lifetime  $\tau(V_g)$  extracted from exciton decay profiles at fixed  $V_g$ . The horizontal dashed line marks

the average exciton lifetime in the metallic regime. In the correlated electronic state of the WS<sub>2</sub> bilayer, the reduced dielectric constant enhances the exciton binding energy in WSe<sub>2</sub> and increases the overlap between electron and hole wavefunctions, leading to a pronounced reduction in lifetime. **c** Dependence of the exciton diffusion length  $L = 2\sqrt{D\tau}$  on doping. The diffusion coefficient  $D$  is obtained from the slope of the variance growth  $\Delta\sigma^2(t) = 4Dt$ . The diffusion length is markedly reduced at fractional fillings, attributed to the combined effects of a shortened exciton lifetime and a decreased diffusion coefficient.

at which this normalized suppression contrast decreases to 10% of its low-temperature value (Supplementary Fig. 26).

The states at the filling factors  $\nu = 1/3$  and  $2/3$  exhibit a higher critical temperature ( $\sim 40$  K), while the state at  $\nu = 1/2$  has a substantially lower  $T_c$  of approximately 20 K. These transitions occur primarily because thermal energy allows electrons to overcome the narrow electronic bandwidth and the long-range Coulomb interactions that stabilize the insulating states at lower temperatures, and thereby restoring exciton transport. Meanwhile, thermal fluctuations promote exciton diffusion in the WSe<sub>2</sub> sensor. These combined effects eliminate the suppression of the diffusivity of the 1 s exciton in WSe<sub>2</sub>, providing insight into the mechanisms that govern exciton dynamics mediated by correlated insulating states.

## Discussion

In summary, we have visualized exciton transport modifications induced by generalized Wigner crystals using ultrafast microscopy combined with a monolayer WSe<sub>2</sub> sensor. By tuning the carrier density in twisted WS<sub>2</sub> moiré superlattices, we drive a transition from a metallic state to a correlated insulating state, which increases dielectric disorder and suppresses exciton transport. This ultrafast optical approach offers a powerful tool for exploring Bose-Fermi mixtures, while maintaining the simplicity and speed of optical measurements. This technique allows access to the electronic density of states near the Fermi surface without requiring electrical contacts, and it can detect changes in the dielectric environment, including metal-insulator or superconducting transitions.

In contrast to conventional exciton sensor techniques that rely on the optical response of 2 s excitons, our method probes dielectric properties through transport and lifetime measurements of 1 s excitons (Supplementary Fig. 27). In 1 s excitons, variations in the dielectric environment shift the quasiparticle bandgap and exciton binding energy in opposite directions, often resulting in an unchanged optical bandgap, as observed in steady-state photoluminescence and reflectance spectra. However, exciton dynamics remain highly responsive to these changes, as the dielectric environment directly affects electron-hole wavefunction overlap. This leads to a pronounced reduction in both exciton lifetime and diffusion length. By capturing these subtle but critical changes, our approach provides a spatio-temporally resolved optical framework that bridges optical and transport measurements, enabling the exploration of quantum phenomena across a broad range of quantum material systems. This, in turn, opens new opportunities for integrating correlated electronic states with excitonic devices, laying the groundwork for multifunctional, dynamically programmable platforms where multiple quasiparticle states coexist.

## Methods

### Device fabrication

The device is assembled layer-by-layer via a dry transfer method, with detailed procedures provided in Supplementary Fig. 28. In brief, few-layer graphite, hBN, monolayer WS<sub>2</sub>, and monolayer WSe<sub>2</sub> flakes are mechanically exfoliated onto silicon substrates with a 285 nm SiO<sub>2</sub> layer. Flakes of appropriate size and thickness are selected according

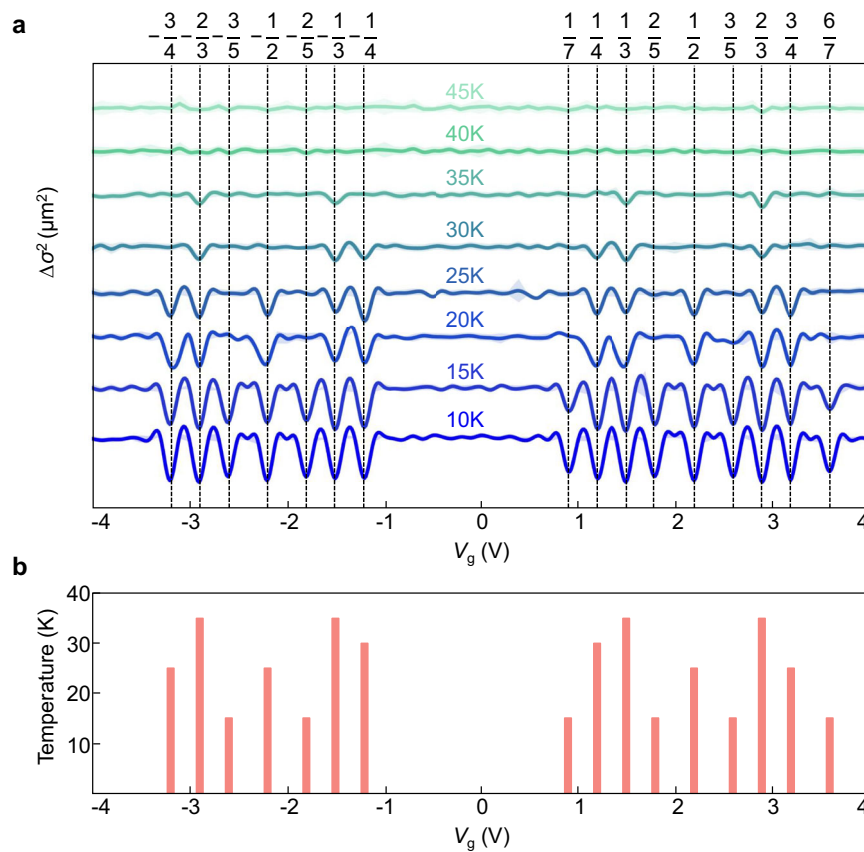


**Fig. 4 | Temperature dependence of exciton transport.** **a** Temperature dependence of exciton transport at 10–45 K with a fixed delay time of 5 ps. At low temperatures, the suppression of exciton transport at fractional fillings is pronounced. As the temperature increases, the overall exciton transport enhances, and the suppression at the fractional fillings progressively diminishes. The shaded areas represent the uncertainty range (error bars), derived from the statistical variation in

the mean-squared displacement  $\Delta\sigma^2(t)$  obtained at three different spatial positions on the same exciton transport map. **b** The critical temperature for transport suppression at different correlated electronic states. The critical values are governed by both the thermal melting of the Wigner crystal and the ability of thermal fluctuations to overcome the moiré potential confinement.

to their optical contrast and PL spectroscopy. The twisted  $\text{WS}_2$  moiré bilayer was fabricated using the tear and stack method<sup>55,56</sup>, in which a portion of the monolayer  $\text{WS}_2$  was torn and rotated in situ, yielding a sample region with an interlayer twist angle of  $58^\circ$ . The twist angle is verified by measuring the moiré period with a lateral force microscope. A monolayer  $\text{WSe}_2$  is then placed near the twisted  $\text{WS}_2$  moiré bilayer, separated by a spacer hBN with a thickness of  $\sim 1$  nm. The contact and gate electrodes consist of few-layer graphite, which is connected to the pre-patterned Pt electrodes on the  $\text{SiO}_2$  layer. The gate dielectric material hBN on each side has a typical thickness of 35–50 nm. To achieve clean interfaces of the heterostructures, the samples were annealed at  $80^\circ\text{C}$  for 8 h in an argon atmosphere, both prior to and following their preparation.

In this device,  $V_g$  is applied to the top graphite gate; the  $\text{WS}_2$  moiré bilayer, the  $\text{WSe}_2$  sensor, and the bottom graphite gate are all grounded. This ground-referenced dual-gate geometry ensures that doping occurs exclusively in the  $\text{WS}_2$  moiré bilayer, while the  $\text{WSe}_2$  sensor remains charge-neutral and reflects only the dielectric screening of the neighboring moiré system.

### Lateral force microscope

Lateral force measurements were performed under ambient conditions (20–25  $^\circ\text{C}$ , relative humidity of 20–30%) using a Cypher atomic force microscope (AFM) from Asylum Research. Probes from Asylum Research (ASYELEC-01) with a nominal radius of approximately 25 nm were employed for these measurements. The lateral force is given by  $F_N = C \cdot k \cdot u$ , where  $C$  refers to the normal force calibration factor of

the probe,  $k$  is the spring constant of the probe, and  $u$  is the voltage applied in the experiment. Both  $C$  and  $k$  are determined by the intrinsic properties of the probe, which can be influenced by factors such as cantilever variations and laser spot positioning. Therefore, it is necessary to calibrate the probe before each experiment to establish an accurate force-to-signal conversion coefficient. The topography map is generated by recording the probe's vertical displacement along with signals in other directions in a  $60 \times 60$  nm square region at a scanning velocity of  $378 \text{ nm s}^{-1}$ . The moiré period is given by  $a_M = a / (2 \sin(\frac{\theta}{2}))$ , which is inversely proportional to the twist angle  $\theta$ . Here  $a = 0.315$  nm is the atomic lattice constant of  $\text{WS}_2$  for  $\theta \sim 58^\circ$  and  $a_M \sim 9.2$  nm.

### Static reflection spectra measurements

A power-stabilized Tungsten-Halogen lamp (Thorlabs, SLS201L) is used as a broadband light source. The output of the lamp is passed through a single fiber and collimated by a collimation. The beam diameter on the sample is about  $1 \mu\text{m}$ , and the beam power is less than 10 nW. The reflected beam is collected by a spectrometer with a diffraction grating of 300 grooves per millimeter. This dispersed beam is detected using a charge-coupled device camera (PYL400-BRX, Princeton Instruments). The reflection contrast spectra,  $\Delta R/R_0 = (R_{\text{sample}} - R_0)/R_0$ , are performed at 4 K, where  $R_{\text{sample}}$  and  $R_0$  are reflection spectrum of the sample and substrate, respectively.

### Femtosecond transient absorption microscopy

Ultrafast absorption microscopy is used to track exciton transport in the monolayer  $\text{WSe}_2$ , with the sample mounted in a closed-cycle

cryostat (Montana Instruments, CA50). A Ti: Sapphire oscillator (Chameleon Ultra II, Coherent) pumps an optical parametric oscillator (Chameleon Compact OPO-Vis, Coherent), generating two independent beams for the pump and probe lights, respectively. The pump wavelength (660 nm) selectively excites WSe<sub>2</sub> without exciting WS<sub>2</sub>, while the probe wavelength (720 nm) monitors the exciton population in WSe<sub>2</sub>. Both beams spatially overlap and are focused onto the sample with a 100× objective (EC Epiplan-Neofluar, 0.9 NA, ZEISS). The reflectance signal is collected through the same objective, filtered to suppress pump leakage and block ambient stray light (center wavelength 740 nm, FWHM ≈ 50 nm), and detected with an avalanche photodiode (APD, C12702-04, Hamamatsu). Pump-induced changes in the probe reflectance ( $\Delta R$ ) are measured by modulating the pump beam at 1 MHz with an acousto-optic modulator (AOM, 3080-125, Gooch Housego), and the APD output is monitored with a lock-in amplifier (HF2LI, Zurich Instruments). The pump-probe delay time is controlled using a mechanical translation stage (DDS600-E/M, Thorlabs). For imaging, a two-dimensional galvanometer (GVS012, Thorlabs) scans the probe beam relative to the pump beam.

### Spatial resolution of transient absorption microscopy

In transient absorption microscopy, the measured exciton transport encompasses contributions from the actual exciton dynamics as well as the spatial profiles of both the pump and probe beams, expressed as  $\sigma^2(\text{measured}) = \sigma^2(\text{change}) + \sigma^2(\text{pump}) + \sigma^2(\text{probe})$ . However, since  $\sigma^2(\text{pump})$  and  $\sigma^2(\text{probe})$  remain nearly constant during the pump-probe delay time, variations in  $\sigma^2(\text{measured})$  primarily reflect changes in the exciton density distribution over time. The primary factor limiting the resolution of these measurements is the signal-to-noise ratio. We can analyse the error of the exciton transport length by differentiating the equation  $L^2 = \sigma_t^2 - \sigma_0^2$  and obtain the expression of the error

$$\Delta L = \sqrt{\frac{\sigma_t^2}{\sigma_t^2 - \sigma_0^2} (\Delta\sigma_t)^2 + \frac{\sigma_0^2}{\sigma_t^2 - \sigma_0^2} (\Delta\sigma_0)^2} = \sqrt{\Delta\sigma_t^2 + \left(\frac{\sigma_0}{t}\right)^2 (\Delta\sigma_0^2 - \Delta\sigma_t^2)},$$

where  $t$  is the pump-probe delay time. As we can see,  $\Delta L$  is determined by  $\Delta\sigma_t$  and  $\Delta\sigma_0$ , which stem from the Gaussian fitting process and the experimental signal-to-noise ratio. Two main noise sources affect transient absorption experiments: laser fluctuation noise and electronic noise from detection systems. To mitigate laser fluctuation noise, lock-in detection is employed, wherein the excitation intensity is modulated using an acoustic-optical modulator. This modulation allows the lock-in amplifier to extract the differential signal at the modulated frequency, effectively reducing low-frequency laser intensity fluctuations. Operating at higher modulation frequencies, such as 1 MHz in our experiments, further minimizes the laser intensity noise, approaching the quantum shot noise limit, which arises from the Poisson distribution of photon numbers at the detector. Accurate demodulation of each pixel necessitates a dwell time significantly longer than the modulation period to ensure precise signal extraction. In our setup, the spatial resolution is approximately 50 nm, determined by the smallest measurable change in the excited-state population profile.

### Determination of the filling factor by exciton transport

The filling factor  $\nu$  is defined as the number of charges per moiré superlattice site,  $\nu = n/n_0$ , where  $n$  is the charge density and  $n_0$  is the moiré density. The moiré density is given by  $n_0 = 2/(\sqrt{3}a_M^2)$ , where  $a_M$  is the moiré lattice constant. For twisted WS<sub>2</sub> with  $\theta \sim 58^\circ$ , we measure the moiré superlattices is about 9.2 nm by atomic force microscopy, which corresponds to an electron density of  $1.36 \times 10^{12} \text{ cm}^{-2}$  at  $\nu = 1$ . The gate-induced charge density  $n$  is estimated from a parallel-plate model,  $n = CV_g/e$ , where  $C$  is the gate capacitance and  $e$  is the elementary charge. The capacitance, dominated by the geometrical capacitance of the gate, is approximately constant and estimated to be  $55 \text{ nF cm}^{-2}$ , based on a 48 nm thick hBN layer with an out-of-plane dielectric constant of about 3. This provides a general estimate of  $\nu$ ,

with uncertainties on the order of 10%, particularly at gate voltages where the exciton transport suppression is small.

To calibrate the filling factor more accurately, we use fractional fillings where exciton diffusion is strongly suppressed as calibration points. At each gate voltage  $V_g$  the spatial profile of exciton transport is fitted with a Gaussian to extract the variance  $\Delta\sigma^2(t)$ , which measures diffusivity. The variance plotted against gate voltage (Fig. 4a) clearly shows distinct drops at some fractional fillings. By matching these voltages with our initial charge-density estimates, we assign them to  $\nu = \pm 1/3, \pm 1/2$  and  $\pm 2/3$ . These insulating states serve as landmarks to estimate a conversion factor between  $V_g$  and  $\nu$  for electrons and holes independently. This procedure avoids the ambiguity of defining  $\nu = 0$  from band edges and ensures that the Fermi level is within the gap. The slopes obtained for both electron and hole doping are nearly identical,  $\alpha \approx 0.25$  carriers per moiré unit cell per volt and this factor is insensitive to temperature up to 40 K. Using this calibration, the remaining insulating states are consistently assigned to the nearest simple rational fractions, typically corresponding to the most stable correlated configurations.

### Mechanism of exciton lifetime in correlated insulating states

The exciton recombination lifetime is strongly affected by the surrounding dielectric environment, as it depends on the exciton binding energy. The binding energy of the 1s exciton is given by  $E_b^1 = (2m_r e^4)/(\hbar^2 (4\pi\epsilon\epsilon_0)^2)$ , where  $\epsilon$  is the dielectric constant,  $\epsilon_0$  is the vacuum permittivity,  $m_r$  is the exciton reduced mass,  $e$  is the elementary charge, and  $\hbar$  is the reduced Planck constant. In the limit of small exciton binding energies, we use the dielectric function in the static limit  $\epsilon(q)$ . Thomas-Fermi screening yields  $\epsilon(q) = \epsilon_b + \frac{e^2}{\epsilon_0 t q^2} \frac{\partial n}{\partial \mu}$  for a uniformly screened Coulomb potential by a free electron gas. Here  $\frac{\partial n}{\partial \mu}$  is the electronic density of states or compressibility,  $\epsilon_b$  is the background dielectric response (from bound charges) and  $t$  is thickness of the 2D layer. The intrinsic radiative lifetime obtained from Fermi's golden rule,  $\tau_{1s}(\epsilon) \propto \frac{\epsilon^2}{E_{1s}(0)m_r^2}$ , where is the 1s exciton resonance energy. When twisted WS<sub>2</sub> enters a correlated insulating state, its dielectric constant decreases, reducing the screening effect and increasing the exciton binding energy. This results in a strong Coulomb interaction between the electron and hole, enhancing the overlap of their wavefunctions, thus significantly shortening the exciton lifetime. As a result, the exciton lifetime in WSe<sub>2</sub> decreases markedly when the adjacent twisted WS<sub>2</sub> layer is in a correlated insulating state.

### Factors influencing exciton dynamics in WSe<sub>2</sub>

In our experiment, we eliminate the influence of both Auger processes and the moiré potential in twisted WS<sub>2</sub> on the exciton dynamics in WSe<sub>2</sub>. First to exclude Auger effects, we employ a low pump power  $P$ , corresponding to an exciton density of  $\sim 1 \times 10^{11} \text{ cm}^{-2}$ , calculated by  $n_{\text{ex}} = (\alpha \cdot P)/(\hbar\omega \cdot f \cdot A)$ , where  $\alpha$  is the absorption coefficient of monolayer WSe<sub>2</sub>,  $\hbar\omega$  is the photon energy,  $f$  is the pulse repetition rate, and  $A$  is the pump beam area. At this density, nonlinear optical effects are negligible, and the exciton lifetime remains constant with increasing power, confirming a linear mechanism. Working in this low-density regime is a necessary condition for subsequently discussing how dielectric disorder influences exciton diffusion<sup>49,51</sup>.

In general, the moiré potential can confine exciton transport, complicating interactions between excitons and correlated insulating states. The moiré potential arises from spatially dependent interlayer hopping between two WS<sub>2</sub> monolayers in direct contact with each other. Interlayer hopping is expected to decay exponentially with layer separation on the atomic length scale. To mitigate moiré potential impact, we introduce a -1 nm thick hBN spacer between the twisted WS<sub>2</sub> and WSe<sub>2</sub> bilayers. The hBN spacer significantly diminishes the moiré potential effect, rendering it negligible. Lateral force

measurements (Fig. 1c and Supplementary Fig. 1) confirm that moiré-induced lateral forces are significant on the bare WS<sub>2</sub> bilayer surface but absent on the hBN spacer surface, indicating that the moiré potential is negligible through the spacer. Importantly, the 1 nm hBN spacer does not block the influence of correlated insulating states in twisted WS<sub>2</sub> on the exciton dynamics in WSe<sub>2</sub>. The Bohr radius of the 1 s exciton in monolayer WSe<sub>2</sub> is approximately 1.7 nm<sup>39,50</sup>—larger than the spacer thickness—allowing the excitons to remain responsive to the dielectric environment of the underlying moiré system. This ensures that our measurements accurately reflect the interaction between excitons and correlated electronic phases in twisted WS<sub>2</sub>.

The WSe<sub>2</sub> layer and the bottom graphite gate are held at ground, and a thin hBN spacer electrically isolates WSe<sub>2</sub> from WS<sub>2</sub>. This geometry keeps WSe<sub>2</sub> charge-neutral while  $V_g$  tunes carriers only in the WS<sub>2</sub> moiré bilayer. If WSe<sub>2</sub> were directly gated or doped, a pronounced, monotonic change in exciton diffusion with  $V_g$  would be expected; this is not observed. In the absence of correlated insulating states, the exciton diffusion essentially remains unchanged.

## Data availability

The data generated in this study are provided in the Supplementary Information/Source Data file. Source data are provided with this paper.

## References

- Qi, R. et al. Perfect Coulomb drag and exciton transport in an excitonic insulator. *Science* **388**, 278–283 (2025).
- Tagarelli, F. et al. Electrical control of hybrid exciton transport in a van der Waals heterostructure. *Nat. Photonics* **17**, 615–621 (2023).
- Sun, Z. et al. Excitonic transport driven by repulsive dipolar interaction in a van der Waals heterostructure. *Nat. Photonics* **16**, 79–85 (2022).
- Datta, K. et al. Spatiotemporally controlled room-temperature exciton transport under dynamic strain. *Nat. Photonics* **16**, 242–247 (2022).
- del Águila, A. G. et al. Ultrafast exciton fluid flow in an atomically thin MoS<sub>2</sub> semiconductor. *Nat. Nanotechnol.* **18**, 1012–1019 (2023).
- Malic, E., Perea-Causin, R., Rosati, R., Erkensten, D. & Brem, S. Exciton transport in atomically thin semiconductors. *Nat. Commun.* **14**, 3430 (2023).
- High, A. A. et al. Spontaneous coherence in a cold exciton gas. *Nature* **483**, 584–588 (2012).
- Jin, C. et al. Imaging of pure spin-valley diffusion current in WS<sub>2</sub>-WSe<sub>2</sub> heterostructures. *Science* **360**, 893–896 (2018).
- Rivera, P. et al. Interlayer valley excitons in heterobilayers of transition metal dichalcogenides. *Nat. Nanotechnol.* **13**, 1004–1015 (2018).
- Jin, C. et al. Ultrafast dynamics in van der Waals heterostructures. *Nat. Nanotechnol.* **13**, 994–1003 (2018).
- Yu, Y. et al. Giant enhancement of exciton diffusivity in two-dimensional semiconductors. *Sci. Adv.* **6**, eabb4823 (2020).
- Cutshall, J. et al. Imaging interlayer exciton superfluidity in a 2D semiconductor heterostructure. *Sci. Adv.* **11**, eadr1772 (2024).
- Rivera, P. et al. Valley-polarized exciton dynamics in a 2D semiconductor heterostructure. *Science* **351**, 688–691 (2016).
- Ahn, H. et al. Integrated 1D epitaxial mirror twin boundaries for ultrascaled 2D MoS<sub>2</sub> field-effect transistors. *Nat. Nanotechnol.* **19**, 955–961 (2024).
- Chen, M. et al. Selective and quasi-continuous switching of ferroelectric Chern insulator devices for neuromorphic computing. *Nat. Nanotechnol.* **19**, 962–969 (2024).
- Kim, K. S. et al. The future of two-dimensional semiconductors beyond Moore's law. *Nat. Nanotechnol.* **19**, 895–906 (2024).
- Meng, K. et al. Superionic fluoride gate dielectrics with low diffusion barrier for two-dimensional electronics. *Nat. Nanotechnol.* **19**, 932–940 (2024).
- Pack, J. et al. Charge-transfer contacts for the measurement of correlated states in high-mobility WSe<sub>2</sub>. *Nat. Nanotechnol.* **19**, 948–954 (2024).
- Wang, Z., Wan, T., Ma, S. & Chai, Y. Multidimensional vision sensors for information processing. *Nat. Nanotechnol.* **19**, 919–930 (2024).
- Yuan, L. et al. Twist-angle-dependent interlayer exciton diffusion in WS<sub>2</sub>-WSe<sub>2</sub> heterobilayers. *Nat. Mater.* **19**, 617–623 (2020).
- Unuchek, D. et al. Room-temperature electrical control of exciton flux in a van der Waals heterostructure. *Nature* **560**, 340–344 (2018).
- Peng, R. et al. Long-range transport of 2D excitons with acoustic waves. *Nat. Commun.* **13**, 1334 (2022).
- Kulig, M. et al. Exciton diffusion and Halo effects in monolayer semiconductors. *Phys. Rev. Lett.* **120**, 207401 (2018).
- Unuchek, D. et al. Valley-polarized exciton currents in a van der Waals heterostructure. *Nat. Nanotechnol.* **14**, 1104–1109 (2019).
- Raja, A. et al. Dielectric disorder in two-dimensional materials. *Nat. Nanotechnol.* **14**, 832–837 (2019).
- Darlington, T. P. et al. Imaging strain-localized excitons in nanoscale bubbles of monolayer WSe<sub>2</sub> at room temperature. *Nat. Nanotechnol.* **15**, 854–860 (2020).
- Dirnberger, F. et al. Quasi-1D exciton channels in strain-engineered 2D materials. *Sci. Adv.* **7**, eabj3066 (2021).
- Choi, J. et al. Moiré potential impedes interlayer exciton diffusion in van der Waals heterostructures. *Sci. Adv.* **6**, eaba8866 (2020).
- Xu, Y. et al. Correlated insulating states at fractional fillings of moiré superlattices. *Nature* **587**, 214–218 (2020).
- Huang, X. et al. Correlated insulating states at fractional fillings of the WS<sub>2</sub>/WSe<sub>2</sub> moiré lattice. *Nat. Phys.* **17**, 715–719 (2021).
- Li, H. et al. Imaging local discharge cascades for correlated electrons in WS<sub>2</sub>/WSe<sub>2</sub> moiré superlattices. *Nat. Phys.* **17**, 1114–1119 (2021).
- Zhang, Z. et al. Correlated interlayer exciton insulator in heterostructures of monolayer WSe<sub>2</sub> and moiré WS<sub>2</sub>/WSe<sub>2</sub>. *Nat. Phys.* **18**, 1214–1220 (2022).
- Regan, E. C. et al. Mott and generalized Wigner crystal states in WSe<sub>2</sub>/WS<sub>2</sub> moiré superlattices. *Nature* **579**, 359–363 (2020).
- Jin, C. et al. Stripe phases in WSe<sub>2</sub>/WS<sub>2</sub> moiré superlattices. *Nat. Mater.* **20**, 940–944 (2021).
- Li, H. et al. Wigner molecular crystals from multielectron moiré artificial atoms. *Science* **385**, 86–91 (2024).
- Tang, Y. et al. Evidence of frustrated magnetic interactions in a Wigner–Mott insulator. *Nat. Nanotechnol.* **18**, 233–237 (2023).
- Nuckolls, K. P. & Yazdani, A. A microscopic perspective on moiré materials. *Nat. Rev. Mater.* **9**, 460–480 (2024).
- Li, H. et al. Imaging two-dimensional generalized Wigner crystals. *Nature* **597**, 650–654 (2021).
- Tang, Y. et al. Dielectric catastrophe at the Wigner–Mott transition in a moiré superlattice. *Nat. Commun.* **13**, 4271 (2022).
- Li, H. et al. Mapping charge excitations in generalized Wigner crystals. *Nat. Nanotechnol.* **19**, 618–623 (2024).
- Li, H. et al. Imaging moiré excited states with photocurrent tunnelling microscopy. *Nat. Mater.* **23**, 633–638 (2024).
- Cui, H. et al. Interlayer Fermi polarons of excited exciton states in quantizing magnetic fields. *Nano Lett.* **24**, 7077–7083 (2024).
- Zeng, Y. et al. Thermodynamic evidence of fractional Chern insulator in moiré MoTe<sub>2</sub>. *Nature* **622**, 69–73 (2023).
- Zeng, Y. et al. Exciton density waves in Coulomb-coupled dual moiré lattices. *Nat. Mater.* **22**, 175–179 (2023).
- Xu, Y. et al. A tunable bilayer Hubbard model in twisted WSe<sub>2</sub>. *Nat. Nanotechnol.* **17**, 934–939 (2022).
- Li, H. et al. Imaging moiré flat bands in three-dimensional reconstructed WSe<sub>2</sub>/WS<sub>2</sub> superlattices. *Nat. Mater.* **20**, 945–950 (2021).

47. Liu, H., Wang, C., Zuo, Z., Liu, D. & Luo, J. Direct visualization of exciton transport in defective few-layer WS<sub>2</sub> by ultrafast microscopy. *Adv. Mater.* **32**, 1906540 (2020).
48. Liu, H. et al. Direct Visualization of Dark Interlayer Exciton Transport in Moiré Superlattices. *Nano Lett.* **24**, 339–346 (2024).
49. Li, Z. et al. Dielectric engineering for manipulating exciton transport in semiconductor monolayers. *Nano Lett.* **21**, 8409–8417 (2021).
50. Stier, A. V. et al. Magneto-optics of exciton Rydberg states in a monolayer semiconductor. *Phys. Rev. Lett.* **120**, 057405 (2018).
51. Zipfel, J. et al. Exciton diffusion in monolayer semiconductors with suppressed disorder. *Phys. Rev. B* **101**, 115430 (2020).
52. Jena, D. & Konar, A. Enhancement of carrier mobility in semiconductor nanostructures by dielectric engineering. *Phys. Rev. Lett.* **98**, 136805 (2007).
53. Tang, Y. et al. Simulation of Hubbard model physics in WSe<sub>2</sub>/WS<sub>2</sub> moiré superlattices. *Nature* **579**, 353–358 (2020).
54. Yan, L. et al. Anomalously enhanced diffusivity of moiré excitons via manipulating the interplay with correlated electrons. *Nat Commun.* **16**, 10569 (2025).
55. Kim, K. et al. van der Waals heterostructures with high accuracy rotational alignment. *Nano Lett.* **16**, 1989–1995 (2016).
56. Cao, Y. et al. Superlattice-induced insulating states and valley-protected orbits in twisted bilayer graphene. *Phys. Rev. Lett.* **117**, 116804 (2016).

## Acknowledgements

This work is supported by the National Natural Science Foundation of China (no. 52425503 (D.L.), 92577105 (H.L.), 52475199 (H.L.), U2541265 (D.L.), 52488101 (J.L.), 52350380 (H.L.)), and National Key R&D Program of China (No. 2025YFF0522200 (H.L.)).

## Author contributions

H.L. contributed to the experimental design, execution, data analysis, and drafting of the original manuscript. S.C., R.H., and S.H. were responsible for sample preparation and conducting the experiments. X.Z., H.X., L.H. and Z.S. performed data analysis and contributed to discussions of the results. J.L. provided guidance and critical insights for the project. D.L. supervised and directed the project, managing all aspects of the research. All authors participated in the writing and approved the final version of the manuscript.

## Competing interests

The authors declare no competing interests.

## Additional information

**Supplementary information** The online version contains supplementary material available at <https://doi.org/10.1038/s41467-026-68868-5>.

**Correspondence** and requests for materials should be addressed to Huan Liu, Jianbin Luo or Dameng Liu.

**Peer review information** *Nature Communications* thanks Yiduo Wang and the other, anonymous, reviewer(s) for their contribution to the peer review of this work. A peer review file is available.

**Reprints and permissions information** is available at <http://www.nature.com/reprints>

**Publisher's note** Springer Nature remains neutral with regard to jurisdictional claims in published maps and institutional affiliations.

**Open Access** This article is licensed under a Creative Commons Attribution-NonCommercial-NoDerivatives 4.0 International License, which permits any non-commercial use, sharing, distribution and reproduction in any medium or format, as long as you give appropriate credit to the original author(s) and the source, provide a link to the Creative Commons licence, and indicate if you modified the licensed material. You do not have permission under this licence to share adapted material derived from this article or parts of it. The images or other third party material in this article are included in the article's Creative Commons licence, unless indicated otherwise in a credit line to the material. If material is not included in the article's Creative Commons licence and your intended use is not permitted by statutory regulation or exceeds the permitted use, you will need to obtain permission directly from the copyright holder. To view a copy of this licence, visit <http://creativecommons.org/licenses/by-nc-nd/4.0/>.

© The Author(s) 2026